

Molecular Dynamics Simulations of the Chemical Modification of Polystyrene through $C_xF_y^+$ Beam Deposition

Inkook Jang and Susan B. Sinnott*

Department of Materials Science and Engineering, University of Florida, Gainesville, Florida 32611-6400

Received: February 17, 2004; In Final Form: June 6, 2004

The chemical modification of polystyrene through the deposition of a beam of polyatomic fluorocarbon ions ($C_3F_5^+$ and CF_3^+) at experimental fluences is studied using classical molecular dynamics simulations with many-body empirical potentials. To facilitate these simulations, a new C–H–F potential is developed on the basis of the second-generation reactive empirical bond-order potential for hydrocarbons developed by Brenner. Lennard-Jones potentials are used to model long-range van der Waals interactions. The incident energy of the ion beam is 50 eV/ion, and it is deposited normal to the surface. The simulations illustrate the important differences in the chemical interactions of these polyatomic ions with the polystyrene. The CF_3^+ ions are predicted to be more effective at fluorinating the polystyrene than $C_3F_5^+$ ions, and the dissociation of the $C_3F_5^+$ ions produce long-lived precursors to fluorocarbon thin film nucleation.

Introduction

Plasma treatments are widely used to chemically modify the surfaces of a variety of materials, including biomaterials, semiconductors, and polymers. It is therefore somewhat surprising that there is much that is not known about the chemistry by which treated surfaces are modified, largely because of the difficulties in monitoring the process experimentally.^{1–5} Computational methods such as molecular dynamics (MD) simulations are therefore an important approach to the enhancement of our understanding of the chemical processes involved in plasma surface treatments, especially to determine the effect of major components of the complex plasma environment.^{4,6–13}

Fluorocarbons are one of the most commonly used materials in plasma treatments of surfaces. For instance, fluorocarbon plasma treatment has been used for reactive ion etching of silicon dioxide during the fabrication of semiconductor devices and for fluorination of polymer surfaces to produce films with high thermal and chemical resistance, high dielectric constants, and low friction coefficients.^{14–19} The experimental deposition of mass-selected fluorocarbon ion beams^{3,4,6,20} has proven to be a useful way of determining the chemical effects associated with polyatomic ions in low-energy fluorocarbon plasma surface treatments.

In this study, MD simulations of the deposition of a beam of polyatomic fluorocarbon ions onto polystyrene (PS) surfaces are performed at experimental fluences to obtain insight into the mechanisms responsible for fluorocarbon thin film growth and the fluorination of the polymer. To facilitate these simulations, a new C–H–F many-body empirical potential is developed on the basis of Brenner's second-generation reactive empirical bond-order (REBO) potential for hydrocarbons.²¹ The details of this potential are presented in the next section, followed by a discussion of the simulation conditions, simulation results, and conclusions.

Computational Details

C–H–F Potential. The C–H reactive empirical bond-order (REBO) potential developed by Brenner was devised from the Abell–Tersoff bond-order potential^{22–24} and has been successfully used to obtain insight into various processes such as molecule–surface collisions, cluster–surface impacts, and the chemical vapor deposition of diamond.^{7,8,25–31} To develop the C–H–F potential described here, two-body parameters for C–F and F–F interactions are adapted from the potential developed by Graves and co-workers,^{32,33} and the H–F interaction parameters are determined from calculations using the semi-empirical AM1 approach.^{34,35} The chemical binding energy E_b is determined using the following equation:

$$E_b = \sum_i \sum_{j(>i)} [V_R(r_{ij}) - b_{ij}V_A(r_{ij})] \quad (1)$$

where $V_R(r)$ and $V_A(r)$ are pair-additive interactions that model the interatomic repulsion and attraction from electron–electron and nuclear–nuclear repulsion and electron–nuclear attraction, respectively. The quantity r_{ij} is the distance between pairs of nearest-neighbor atoms i and j , and b_{ij} is a bond-order term that takes into account the many-body interactions between atoms i and j , including those due to nearest neighbors and angle effects.

The functions used for $V_R(r)$ and $V_A(r)$ are the same as those used in the second-generation version of the REBO potential developed by Brenner and co-workers for hydrocarbons:²¹

$$V_R(r) = f_c(r) \left(1 + \frac{Q}{r} \right) A e^{-\alpha r} \quad (2)$$

$$V_A(r) = f_c(r) \sum_{n=1,3} B_n e^{-\beta_n r} \quad (3)$$

where A , B , Q , α , and β are two-body parameters. Some of these are adopted from the C–H second-generation REBO,²¹ and some are adopted from the C–F and F–F potentials developed by Graves and co-workers.³³ All of the parameters used here are given in Table 1. The function $f_c(r)$ is also adopted

* To whom correspondence should be addressed. E-mail: sinnott@mse.ufl.edu.

TABLE 1: Two-Body Parameters Used in Equations 1–4 and 6^a

	C–C	C–H	H–H	C–F	F–F	H–F
A (eV)	10953.54416	149.940987	32.817356	909.2022	16451.97	887.0513
B_1 (eV)	12388.79198	32.355186	29.632593	219.7799	146.8149	571.1737
B_2 (eV)	17.567406	0	0	0	0	0
B_3 (eV)	30.714932	0	0	0	0	0
Q (Å)	0.313460	0.340776	0.370471	0	0	0
α (Å ⁻¹)	4.746539	4.102550	3.536299	3.7128	6.8149	3.7789
β_1 (Å ⁻¹)	4.720452	1.434458	1.715892	2.1763	2.8568	3.0920
β_2 (Å ⁻¹)	1.433213					
β_3 (Å ⁻¹)	1.382691					
D_{\min} (Å)	1.7	1.3	1.1	1.7	1.7	1.3
D_{\max} (Å)	2.0	1.8	1.7	2.0	2.0	1.8
R^e		1.09	0.7416	1.2718	1.4119	0.9378

^a Parameters for C–C, C–H, and H–H are adopted from the second-generation REBO potential developed by Brenner and co-workers,²¹ and C–F and F–F parameters are adopted from the C–F potential developed by Graves and co-workers.^{32,33}

TABLE 2: Values of P from Equation 6 at the Integer Points Used for Cubic Spline Interpolation^a

N^H	N^C	N^F	P_{CC}	N^H	N^C	N^F	P_{CH}	N^H	N^C	N^F	P_{CF}
0	0	2	0.00881	0	0	1	0.20934	0	0	1	0.19024
1	0	1	0.00347	0	0	2	-0.05233	0	0	2	0.34857
0	0	3	0.00191	1	0	1	-0.05912	1	0	1	0.33900
1	0	2	-0.00855	0	0	3	-0.28246	1	0	0	0.19024
2	0	1	-0.00577	1	0	2	-0.29589	2	0	0	0.32997
0	1	1	0.00341	2	0	1	-0.30337	0	0	3	-0.30393
0	1	2	-0.00030	0	1	1	-0.12567	1	0	2	-0.31297
1	1	1	-0.00068	0	1	2	-0.28383	2	0	1	-0.31401
0	2	1	0.00153	1	1	1	-0.29783	3	0	0	-0.30555
				0	2	1	-0.31230	0	1	0	0.35000
								0	2	0	0.40311
								0	1	1	0.13292
								1	1	0	0.13300
								0	1	2	-0.29218
								1	1	1	-0.29100
								2	1	0	-0.27497
								0	3	0	0.06844
								0	2	1	-0.20259
								1	2	0	-0.18290

^a For P_{CF} , the values that are not listed are equal to zero.

from the second-generation REBO potential and limits the range of the covalent interactions to ensure that the interactions include only nearest neighbors within a certain range of distances, which are determined by eq 4.²¹

$$f_c(r_{ij}) = 1 \quad r < D_{ij}^{\min}$$

$$f_c(r_{ij}) = \frac{1 + \cos\{(r - D_{ij}^{\min})/(D_{ij}^{\max} - D_{ij}^{\min})\}}{2} \quad D_{ij}^{\min} < r < D_{ij}^{\max} \quad (4)$$

$$f_c(r_{ij}) = 0 \quad r > D_{ij}^{\max}$$

where the term $D_{ij}^{\max} - D_{ij}^{\min}$ defines the distance over which the function varies from 1 to 0. The values of D^{\max} and D^{\min} are shown in Table 1.

The bond-order term is calculated using

$$b_{ij} = \frac{1}{2}[b_{ij}^{\sigma-\pi} + b_{ji}^{\sigma-\pi}] + b_{ij}^{\pi} \quad (5)$$

where $b_{ij}^{\sigma-\pi}$ and $b_{ji}^{\sigma-\pi}$ represent the local coordination and bond angles of atoms i and j , respectively.^{21,26} The functional form is the same as that in the second-generation REBO but is modified to allow for F neighbors:

$$b_{ij}^{\sigma-\pi} = [1 + \sum_{k(\neq i,j)} f_c(r_{ik}) G(\cos(\theta_{ijk})) e^{\lambda_{ijk}[(r_{ij} - R_{ij}^e) - (r_{ik} - R_{ik}^e)]}] + P_{ij}(N_i^H, N_i^C, N_i^F)^{-1/2} \quad (6)$$

where $G(\cos(\theta_{ijk}))$ controls the influence of the nearest neighbors on the bond order according to the bond angle among atoms i , j , and k and λ is a fitting parameter used to describe three-body transition states around H and F atoms. The same λ value of 4.0 is used for F and H atoms,²¹ and λ is zero for C atoms. The function P is a correction term that accounts for the different chemistry of C, H, and F around atom i . In particular, the values of N_i^C , N_i^H , and N_i^F represent the number of C, H, and F atoms, respectively, that are nearest neighbors of atom i . The function P is not defined analytically, but the values are determined by cubic spline interpolation with some predetermined values. In this work, some new parameters are generated for the P function to include the effect of F atoms. Values at the knots for spline interpolation are determined using the semiempirical AM1 method^{34,35} by fitting to atomization energies of model structures, and the parameters used for the P function for hydrocarbons only are unchanged from the values in the second-generation REBO potential.²¹ The values used to generate the new parameter sets are given in Table 2.

The function b_{ij}^{π} in eq 5 is introduced to describe conjugated systems, radical character, and the influence of dihedral angles in C–C double bonds.²¹ It has the form

$$b_{ij}^{\pi} = \Pi_{ij}^{\text{RC}} + \Pi_{ij}^{\text{DH}} \quad (7)$$

where Π_{ij}^{RC} describes conjugated systems and radical character between atoms i and j as

$$\Pi_{ij}^{\text{RC}} = Y_{ij}(N_i^t, N_j^t, N_{ij}^{\text{conj}}) \quad (8)$$

TABLE 3: Atomization Energies of Various Molecules Calculated with the New C–H–F Potential and the Semiempirical (PM3) Method^a

molecule	C–H–F REBO (eV)	semiempirical (PM3) (eV)
CF ₄ *	19.81	20.44
CHF ₃ *	19.48	19.15
CH ₂ F ₂ *	19.08	18.06
CH ₃ F*	18.63	17.34
CF ₃ *	14.70	15.65
CHF ₂ *	14.28	14.63
CH ₂ F*	13.84	13.68
C ₂ F ₆ *	33.07	33.50
CHF ₂ CHF ₂ *	32.53	31.37
CH ₂ FCH ₂ F*	31.56	29.85
C ₂ F ₄ *	25.89	25.39
CHFCHF*	25.20	25.39
C ₂ F ₂ *	18.27	16.69
CHCF	17.92	17.11
CF ₂ CF ₂	34.63	32.72
CF ₂ CFCF ₃	39.13	39.12
CFCFCF ₃	33.66	34.12
CF ₂ CCF ₃	34.05	34.23
CF ₃ CF ₂ CF ₃	46.21	46.74
CH ₂ FCHFCHF ₂	44.91	43.13
CF ₃ CF ₂ CF ₂ CF ₃	59.22	59.98
CF ₃ CFCFCF ₃	52.33	52.68
CH ₂ FCFCHCHF ₂	51.29	49.70
CHF ₂ CHFCHFCH ₂ F	57.77	55.67
C ₆ F ₁₂ (cyclo)*	77.74	79.51
C ₆ H ₆ F ₆ (cyclo)*	76.96	74.98
C ₆ F ₆ (cyclo)	59.44	59.30

^a Molecules indicated with a * were included in the potential development.

and Π_{ij}^{DH} depends on the dihedral angles in C–C double bonds.²¹ The values of the function Y are determined by tricubic spline interpolation as function P . N_i^t and N_j^t are the total number of neighboring atoms around atoms i and j , respectively, regardless of their type. N_{ij}^{conj} depends on local conjugation and is expressed as

$$N_{ij}^{\text{conj}} = 1 + \left[\sum_{k(\neq i,j)}^{\text{carbon}} f_c(r_{ik}) F(x_{ik}) \right]^2 + \left[\sum_{l(\neq i,j)}^{\text{carbon}} f_c(r_{jl}) F(x_{jl}) \right]^2 \quad (9)$$

$$x_{ik} = N_k^t - f_c(r_{ik}) \quad (10)$$

$$F(x) = \begin{cases} 1 & x < 2 \\ [1 + \cos\{2\pi(x - 2)\}]/2 & 2 < x < 3 \\ 0 & x > 3 \end{cases} \quad (11)$$

The term Π_{ij}^{DH} in eq 7 has zero value if either atom i or j is not carbon. It has the form of

$$\Pi_{ij}^{\text{DH}} = T_{ij}(N_i^t, N_j^t, N_{ij}^{\text{conj}}) \left[\sum_{k(\neq i,j)} \sum_{l(\neq i,j)} \{1 - \cos^2(\Theta_{ijkl})\} f_c(r_{ik}) f_c(r_{jl}) \right] \quad (12)$$

where $\Theta_{ijkl} = e_{jik}e_{ijl}$ and values of the function T are determined by tricubic spline interpolation. Functions e_{jik} and e_{ijl} are unit vectors in the direction of the cross products $\mathbf{R}_{ji} \times \mathbf{R}_{ik}$ and $\mathbf{R}_{ji} \times \mathbf{R}_{il}$, respectively. \mathbf{R}_{ji} is a vector that connects atoms j and i .²¹

In b_{ij}^{π} , a fluorine atom can be described in the same way as a hydrogen atom. Therefore, the formulation of this function is unchanged from the second-generation REBO and is unaffected by the addition of F.

In Table 3, atomization energies of various molecules calculated with the new C–H–F potential are compared with

TABLE 4: Surface Density of Indicated Species that Remain Bonded to Carbon Atoms In, or Are Embedded within, the PS Surfaces after C₃F₅⁺ Deposition^a

	density ($\times 10^{13} \text{ cm}^{-2}$)	
	covalently bonded	embedded
C ₃ F ₅	6.1	44.1
C ₃ F _n (except C ₃ F ₅)	3.0	3.0
C ₂ F _n	7.6	9.1
CF ₂	10.6	9.1
CF	1.5	1.5
C _n F _m ($n > 3, m > 5$)	0	6.1
F	4.6	13.7

^a “Embedded” means that the species are simply embedded in the surface on the time scales of the simulations.

TABLE 5: Surface Density of Indicated Species that Remain Bonded to Carbon Atoms In, or Are Embedded within, the PS Surfaces after CF₃⁺ Deposition

	density ($\times 10^{13} \text{ cm}^{-2}$)	
	covalently bonded	embedded
CF ₄	0	7.6
CF ₃	19.8	36.5
CF ₂	38.0	24.3
CF	4.6	0
C ₂ F _n	4.6	10.6
F	109.4	13.7
F ₂	0	1.5

TABLE 6: Yield of Scattering Species for CF₃⁺ Deposition^a

species	CF ₃	CF ₂	CF	F ₂	F	C _n F _m
yield (%)	33.0	23.5	2.0	2.0	10.8	4.8

^a $n > 1, m > 2$.

TABLE 7: Yield of Scattering Species for C₃F₅⁺ Deposition

species	C ₃ F ₅	C ₃ F ₄	C ₂ F ₃	C ₂ F ₂	CF ₂	CF	F
yield (%)	32.5	3.8	14.6	7.5	20.8	5.8	8.8

the energies obtained by semiempirical (PM3) calculations. The discrepancy between two sets of data is not larger than 10% for these molecules. Bond distances and bond angles have also been checked, and the differences are less than or equal to 10%.

Simulation Details. The MD simulations numerically integrate Newton’s equations of motion with a third-order Nordsieck predictor corrector³⁶ using a time step of 0.2 fs. Short-range interatomic forces are calculated using the new C–H–F potential. Long-range van der Waals interactions are included in the form of a Lennard-Jones potential³⁶ that is active only at distances greater than the covalent bond lengths.

Because of the empirical, classical nature of these potentials, electronic effects such as electronic excitations or charging of the atoms are not included. Therefore, ions with positive charges are treated as reactive radicals rather than true ions with an actual charge. This approach assumes that the incident ions are rapidly neutralized as they approach the surface. The spontaneous neutralization of ions on an insulating surface may not be as intuitive an assumption as it is on a conducting surface. However, the neutralization of ions on insulating surfaces is possible by the Auger process.^{37,38} Experimentally, charge build-up on the surface is a more significant problem that can be negated by techniques such as electron beam irradiation. The simulations reported here, therefore, do not consider the deceleration of ions by accumulated charge.

The polymer surface used in the simulations is syndiotactic crystalline polystyrene and contains eight layers for a total

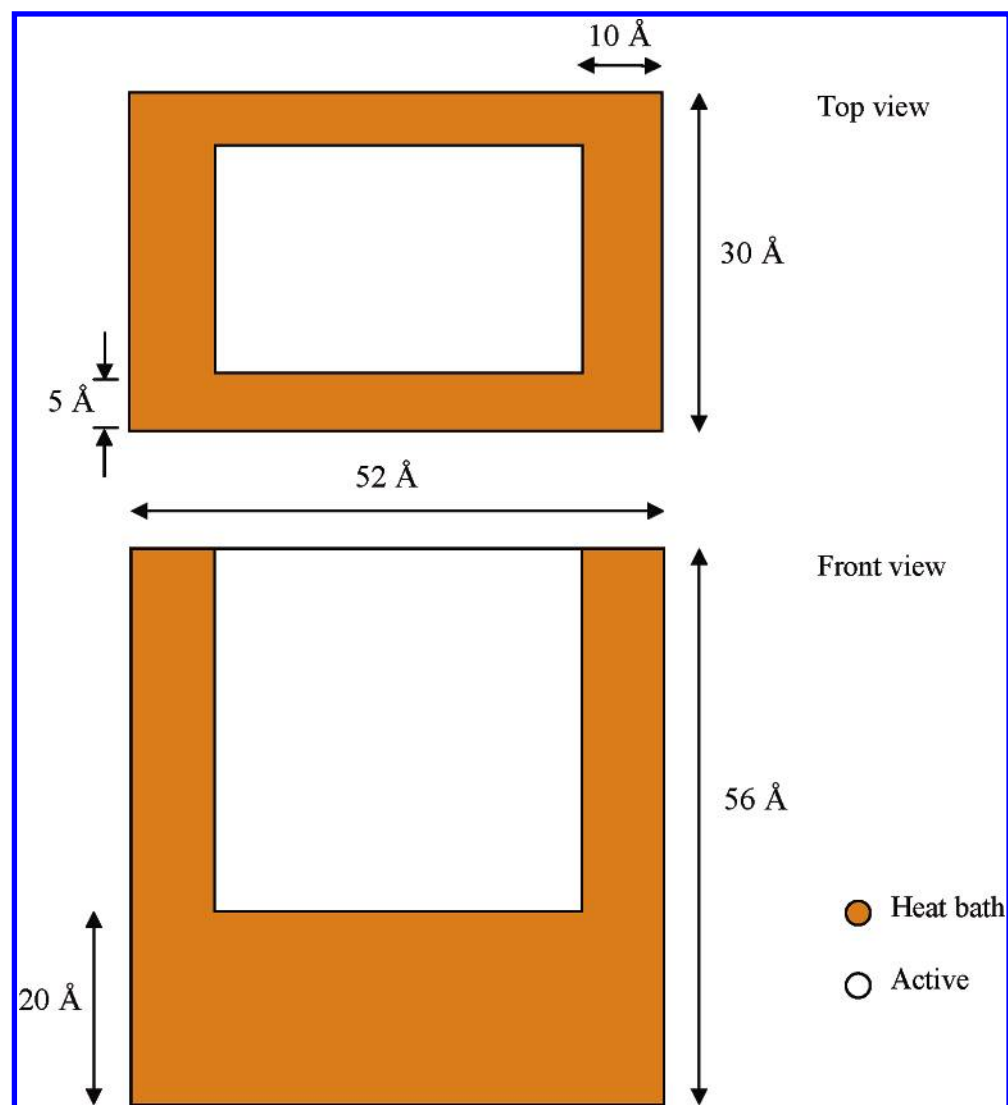


Figure 1. Schematic representation of the PS substrate system.

thickness of 56 Å. The total number of atoms in the system is approximately 10 000. The PS chains are aligned along the short side of the slab (30 Å), and 12 repeat units ($-\text{CH}_2-\text{CHC}_6\text{H}_5-$) fit in this length. The three bottom layers of the surface and atoms within 5–10 Å from the four sides of the slab have Langevin frictional and stochastic forces³⁶ applied to maintain the surface temperature at 300 K. This imitates the heat dissipation process of real surfaces. The rest of the atoms in the system have no constraints and are designated as “active”. Periodic boundary conditions³⁶ are also applied within the plane of the surface to mimic an infinite surface. Figure 1 provides a schematic representation of the PS surface system.

After the system is relaxed at 300 K for 3 ps, a beam of 240 C_3F_5^+ ions ($\text{CF}_2-\text{C}^+\text{F}-\text{CF}_2$) or a beam of 400 CF_3^+ ions is deposited on the PS substrate with the dimensions shown in Figure 1. Each ion in the continuous beam is deposited at randomly chosen locations within the active region of the surface at random orientations relative to the surface. The total kinetic energy of the ions is 50 eV, and the incident angle is along the surface normal. In both cases, the total fluence is equal to 1.8×10^{16} F atom/ cm^2 , which is the same as experimental values corresponding to ion currents of 80 nA.⁴ After the ion beam deposition process is complete, the systems are equilibrated for 25 ps.

Results and Discussion

Figure 2 shows the PS models after the deposition of the C_3F_5^+ and CF_3^+ ion beams and the subsequent equilibration. No distinct fluorocarbon film layers are predicted to form on the time scales of these simulations. Rather, numerous fluorocarbon ions and dissociated ion fragments are embedded in the PS, some of which form covalent bonds to PS carbon atoms. The polymer backbone structures are randomized; consequently, their volume increases by ion bombardment. Because of the higher incident ion velocities and consequently larger transfer of energy to the surface, CF_3^+ ion deposition induces more disordering and swelling of the PS than C_3F_5^+ ion deposition. Surface etching yields are approximately the same for the two ions at 0.26 C atom/ion and 0.29 H atom/ion for C_3F_5^+ and 0.28 C atom/ion and 0.31 H atom/ion for CF_3^+ . However, total F uptake and deposition yield are higher for CF_3^+ than for C_3F_5^+ at 4.29×10^{15} F atoms/ cm^2 and 5.12×10^{15} atoms/ cm^2 for C_3F_5^+ and CF_3^+ , respectively. Deposition yields are 23.2% C and 23.5% F by C_3F_5^+ and 26.5% C and 28.1% F by CF_3^+ . This result can be attributed to the size difference between C_3F_5^+ and CF_3^+ as well as the difference in their incident velocities. In other words, more ions and ion fragments scatter away from the PS surface during C_3F_5^+ ion beam deposition because of

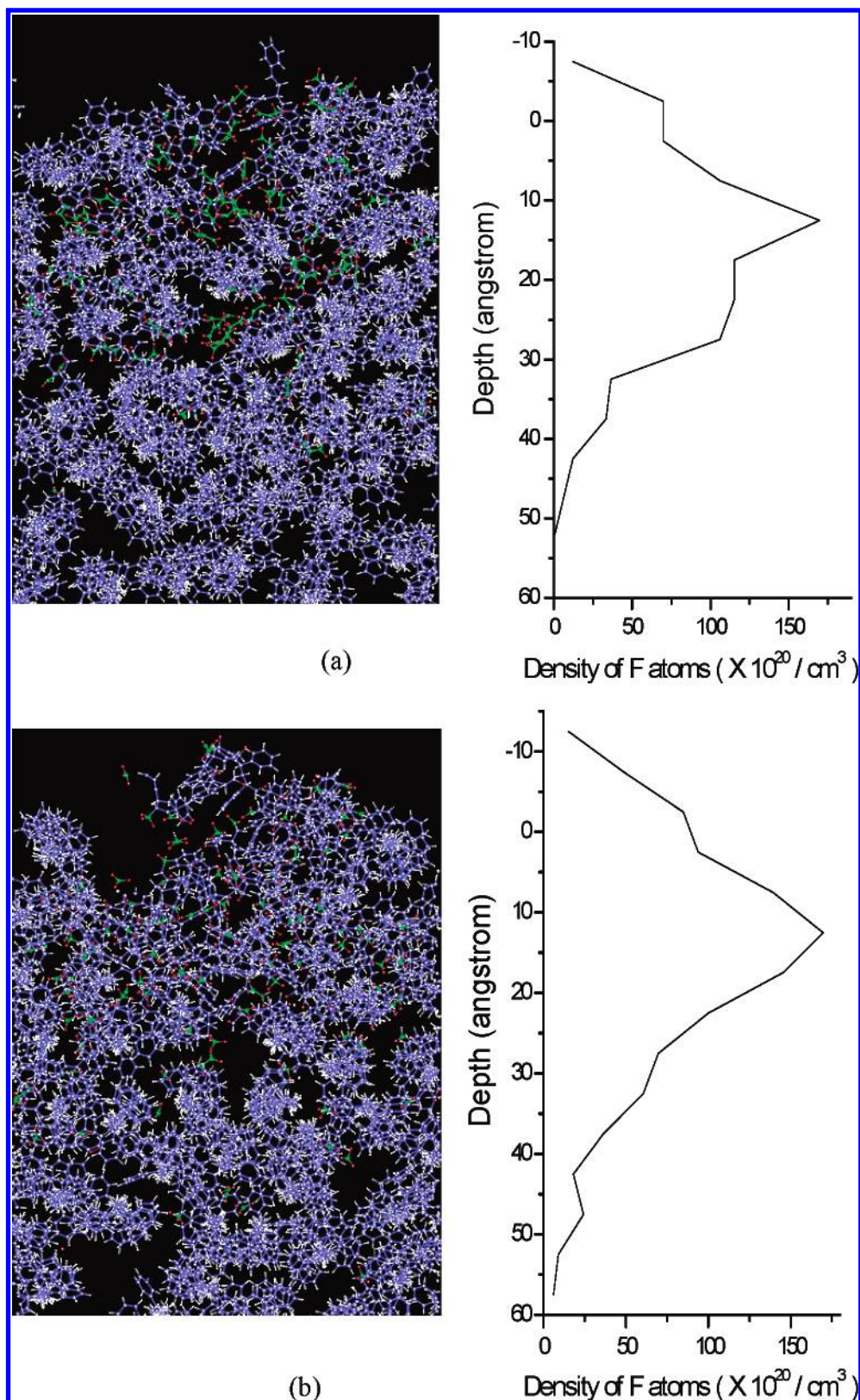


Figure 2. Structure models of PS surfaces (red spheres are F atoms, green spheres are C atoms from the ions, blue spheres are C atoms from the PS, and white spheres are H atoms). (a) Snapshot of the PS surface after $C_3F_5^+$ ion beam deposition and equilibration and depth profile of F density in the PS surface. (b) Snapshot of the PS surface after CF_3^+ ion beam deposition equilibration and depth profile of F density in the PS. The vertical scales of the depth profile graphs are matched with the snapshots. The negative depth corresponds to swelling of the PS surfaces, as discussed in the text. Zero depth corresponds to the initial surface level of the pristine substrates.

the larger size and lower velocities of the ions compared to those in the CF_3^+ ion beam.

Figure 2 also shows F density depth profiles in the PS after ion deposition is complete. The cause of the apparent negative

depth is the swelling of the PS surfaces. (Zero depth is the initial level of the pristine surfaces.) The F atoms spread slightly more widely and deeply as a result of CF_3^+ ion beam deposition than $C_3F_5^+$ ion beam deposition because of the smaller size and

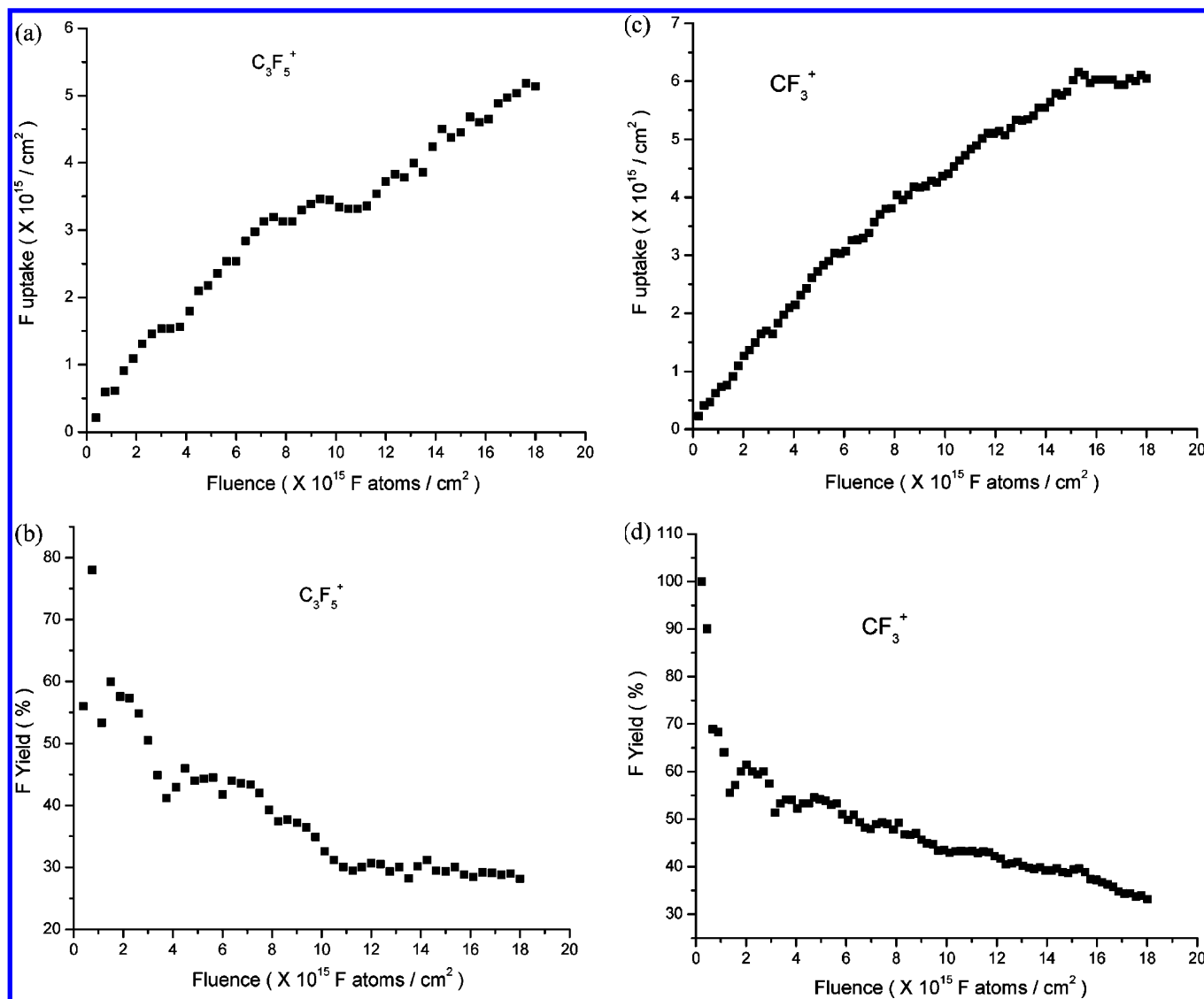


Figure 3. F uptake and total deposition yield of F (number of remaining F atoms per incoming F atoms) as a function of fluence during deposition. (a) F uptake for $C_3F_5^+$ deposition. (b) Deposition yield of F for $C_3F_5^+$ deposition. (c) F uptake for CF_3^+ deposition. (d) Deposition yield of F for CF_3^+ deposition.

higher velocity of the CF_3^+ . However, the highest density of F occurs at a depth of 10–15 Å for both $C_3F_5^+$ and CF_3^+ ion beams. The average penetration depths of F and C atoms are also very similar. Specifically, the average penetration depths are 16.0 Å for both C and F atoms after $C_3F_5^+$ ion deposition and 15.9 and 15.2 Å for C and F, respectively, in the case of CF_3^+ ion deposition. More F atoms chemically bond to the PS during CF_3^+ ion deposition than during $C_3F_5^+$ ion deposition, as shown in Tables 3 and 4. In general, ions or ion fragments that form covalent bonds with the polymer substrate have smaller penetration depths than nonbonded, embedded species. This explains why the penetration depths of F atoms for CF_3^+ deposition are similar to the penetration depths for $C_3F_5^+$ deposition. Thus, with regard to the depth of surface modification, CF_3^+ deposition is approximately equivalent to $C_3F_5^+$ deposition under conditions of experimental fluence where the CF_3^+ ions have higher incident velocities than the $C_3F_5^+$ ions.

Despite these similarities in the overall results between $C_3F_5^+$ and CF_3^+ ion beam deposition processes, the simulations predict that the detailed fluorination mechanisms of the PS surface by the $C_3F_5^+$ and CF_3^+ ions are very different from one another, as shown in Tables 4 and 5. Intact C_3F_5 that is simply embedded within the substrate is the most abundant species in the PS

surface deposited for $C_3F_5^+$ ion beam deposition and corresponds to over 11% of incident $C_3F_5^+$. CF_2 is one of the most reactive ion fragments, with over 50% of deposited CF_2 forming covalent bonds with PS chains. For CF_3^+ deposition, F bonded to a PS chain is the most frequently observed particle and corresponds to 6% of all incident F atoms. These F atoms are attached to the PS chains by replacing H atoms within the PS structure or capping the ends of broken chains. CF_2 is again found to be one of the major reactive ion fragments.

There is some controversy about the role of CF_x (especially CF_2) in fluorocarbon film deposition on Si and SiO_2 surfaces from plasma. Spectroscopic analysis indicates that CF_2 fragments are major building blocks of fluorocarbon films,^{18,39} and some researchers correlate adsorbed CF_2 with gas-phase CF_2 .^{39–41} This suggests that the direct deposition of CF_2 plays a major role in fluorocarbon film growth. However, other researchers argue that there is no direct correlation between gas-phase CF_2 and fluorocarbon film growth.^{5,18,42} In these simulations, CF_2 fragments are found to be the second most abundant and reactive species produced, regardless of the type of ion in the beam. In the case of $C_3F_5^+$, over 50% of the deposited CF_2 fragments form covalent bonds with the PS chains, and in the case of CF_3^+ , 61% of the deposited CF_2 ions form covalent bonds with the

PS chains. Furthermore, because CF_2 has two active sites, it can act as a cross-linking agent between neighboring PS chains. Some cross links are predicted to form within the PS. Thus, these MD simulations indicate that when either C_3F_5^+ or CF_3^+ polyatomic ions are deposited on a surface a significant number of CF_2 ion fragments are generated that react with the surface. Although the substrates in these simulations are polymeric rather than Si or SiO_2 , these results are consistent with reported spectroscopy results^{4,6} and support the argument that fluorocarbon films are not formed exclusively by the direct interaction of gaseous CF_2 with the surface. Rather, our simulations predict that CF_2 species are readily formed by the dissociation of polyatomic ions in surface collisions.

Tables 6 and 7 show the yields of the major scattering species for CF_3^+ and C_3F_5^+ ion beam deposition, respectively. In the case of CF_3^+ ion deposition, CF_3 , CF_2 , and F are the major scattering species. The scattering data for CF_3^+ ion deposition agrees with reported experimental results that show that relative amounts of CF_3 , CF_2 , CF, and F depend on the incident energy of the ion, and more CF and fewer CF_3 species emerge as scattering fragments at higher incident energy.^{43–45} Although the simulations do predict that fewer CF scattering fragments are produced than in experimental results from a gold surface coated with a monolayer of $\text{CF}_3(\text{CF}_2)_{11}(\text{CH}_2)_2\text{SH}$ at the same incident energy,⁴⁵ this difference is attributed to the fact that different surfaces are considered in the simulations and experiments. For example, polymer chains can be locally deformed by bond rotation and stretching and can therefore distribute excess energy throughout a relatively wide area because there is free space between chains. In metals, however, local deformation is almost always accompanied by bond-breaking and, for example, dislocation generation.

In the case of C_3F_5^+ deposition, C_3F_5 , C_2F_3 , and CF_2 are the major scattering species. Combined with the data shown in Table 4, this result indicates that most of the ion dissociation occurs by breaking one of the C–C bonds in the incident C_3F_5^+ . Some experiments for a gold surface coated with a monolayer of $\text{CF}_3(\text{CF}_2)_{11}(\text{CH}_2)_2\text{SH}$ under similar conditions find that CF_3 is a major scattering fragment and no significant amount of CF_2 is detected, in disagreement with our results.⁴⁵ However, this experimental system contains CF_3 units prior to fluorocarbon deposition, while the system considered in the simulations does not. Other experiments on systems more closely related to those examined in these simulations find that CF_2 is a major fragment and little CF_3 is detected, in good agreement with our results.⁴ In these simulations, the ground state of C_3F_5^+ ($\text{CF}_2\text{—C}^+\text{F—CF}_2$) is used. However, a higher-energy-state isomer, such as $\text{CF}_3\text{—C}^+ = \text{CF}_2$ or $\text{CF}_3\text{—CF—C}^+\text{F}$ is possible, and these have CF_3 moieties. In a previous study, we explored the effect of different structures of C_3H_5^+ on the results of deposition on polystyrene and found that if the incident ion contains CH_3 moieties then CH_3 fragment are preferentially produced as major species by dissociation.⁴

In Figure 3, the F atom uptake and total deposition yield are presented. For C_3F_5^+ deposition, the amount of F uptake increases continuously though the deposition yields decrease at high fluence, converging to 29% at the later stage of deposition. This implies that the fluorocarbon film will be continuously built up as the process progresses. It has been reported that fluorocarbon films are maintained at constant levels from a certain stage of the deposition process onward when the fluorocarbon ion beams are deposited on Si surfaces at 100 eV.³³ Unlike the high-energy ion deposition on hard surfaces such as Si, it is more likely that unlimited film growth occurs on

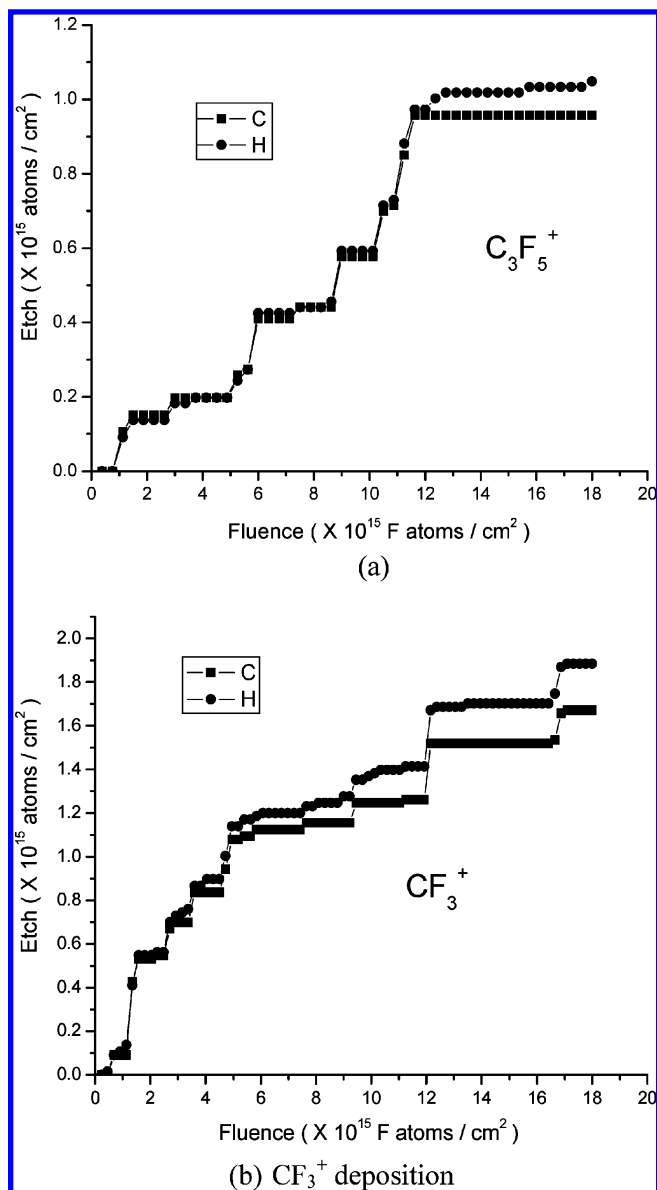


Figure 4. Degree of PS surface etching during ion beam deposition.

relatively soft polymer surfaces by low-energy ion deposition. At the stage where the deposition yield starts to converge to a constant value, the surface etching also decreases, as shown in Figure 4a for the C_3F_5^+ deposition processes. Therefore, it appears that this system is approaching a steady-state, continuous film growth stage after an induction period.

For CF_3^+ deposition, Figure 3 shows that the deposition yield decreases continuously to the final deposition stage without any sign of leveling off. Additionally, it appears that the amount of F uptake tends to converge to a constant value at the latter stages of the deposition process. However, the final deposition yield of CF_3^+ is still large, and the plateau in Figure 3c might be temporary because such a plateau is also briefly seen in Figure 3a. Figure 4b shows that the etching process is still developing at the final stage of deposition though the rate keeps decreasing. Therefore, the CF_3^+ deposition process does not reach steady state on the time scale of these simulations.

It should be pointed out that the final values of F uptake in Figure 3 are higher than the total fluorine density summed from Tables 4 and 5 because the values presented earlier are obtained after long equilibration processes. During equilibration, more than 15% of the deposited F atoms are desorbed from both PS

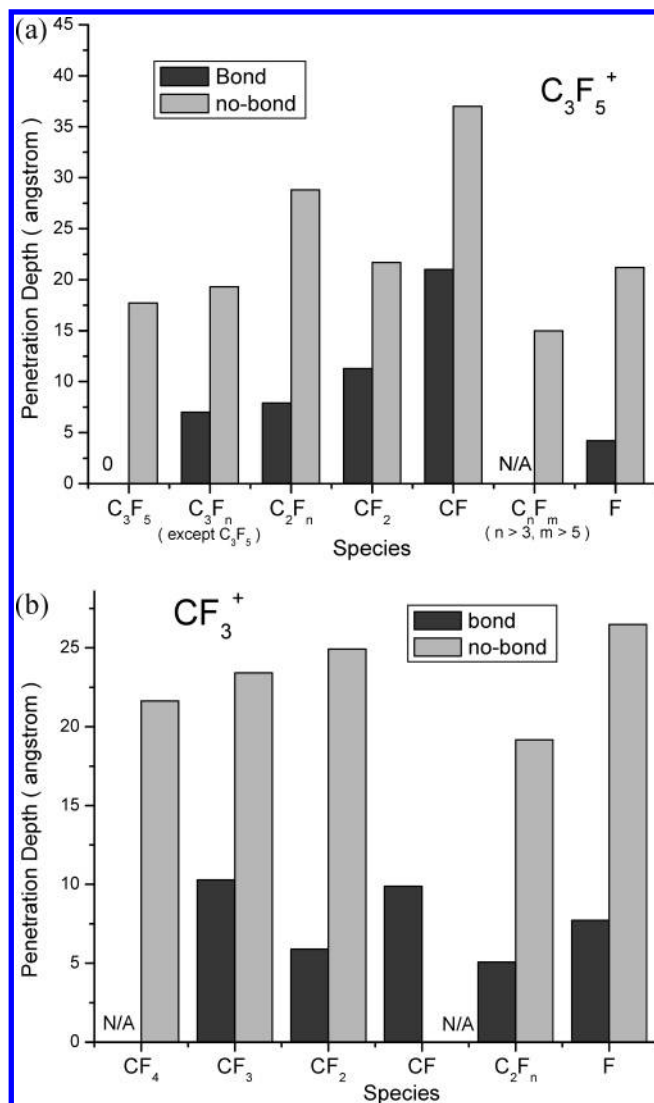


Figure 5. Average penetration depths of indicated species in the PS surfaces. “Bond” means that the species form covalent bonds with C atoms in the PS chains, and “no-bond” means the species are simply embedded in the surface on the time scales of the simulations. (a) $C_3F_5^+$ deposition. (b) CF_3^+ deposition

surfaces treated with $C_3F_5^+$ and CF_3^+ . Most of the desorbed F atoms were simply embedded in the surface before equilibration and were thus not covalently bonded to the PS surface.

Figure 5 shows the average penetration depths for the major species on the PS surfaces. Zero penetration depth of bonded C_3F_5 means that those particles stay right on the surface. As mentioned previously, a variety of ions and ion fragments that form covalent bond to PS chains show much smaller penetration depths than the same species that is simply embedded in the substrate. Therefore, three dominant species in CF_3^+ deposition, F, CF_2 , and CF_3 , that bond to PS chains have penetrations depths that are equal to less than 10 Å. Thus, these species are very effective at fluorinating the PS surface. For $C_3F_5^+$ ion deposition, the dominant species that are bonded to PS chains, CF_2 , C_2F_n , and C_3F_5 , show penetration depths of 11, 8, and 0 Å, which also makes them effective fluorinators of the PS surface. Although some of these fragments are predicted to remain on, or embedded in, the surface without forming covalent bonds to the PS, these embedded species are expected to form bonds to the PS or with other fragments over longer times than are accessible in these classical MD simulations. Alternatively, C_2F_n and C_3F_5 can be thought of as more effective precursors for

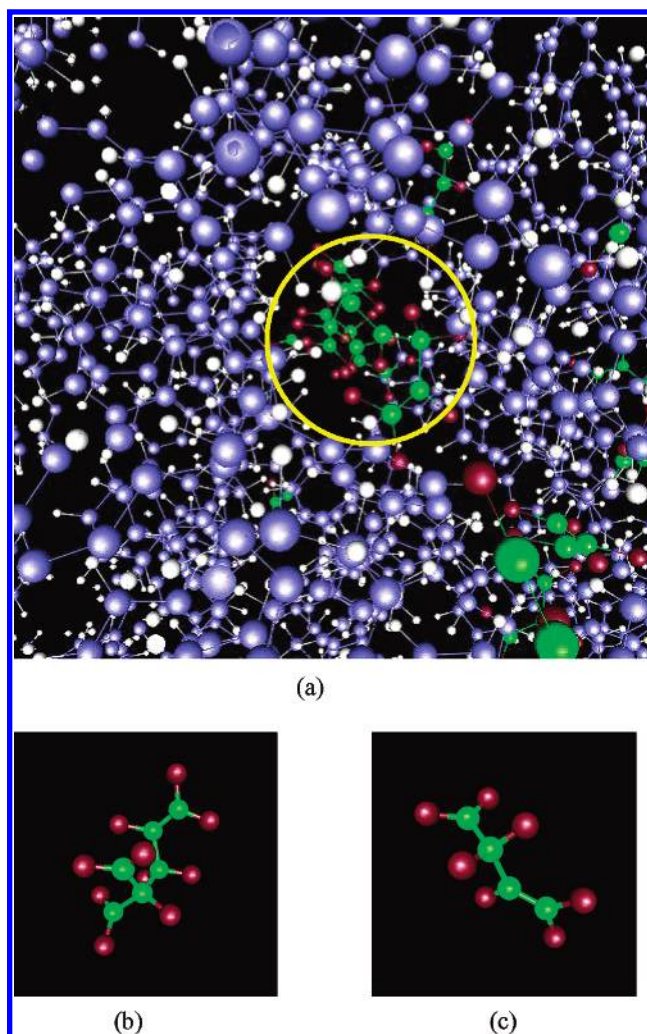


Figure 6. Portion of the PS structure after the deposition of 240 $C_3F_5^+$ ions. (a) Precursors of fluorocarbon polymer within the PS. (b and c) Some precursors shown on their own for clarity. The color schemes are the same as in Figure 1.

fluorocarbon polymer film growth than smaller fragments because they contain more than one carbon atoms and may have more than one active site. These larger fragments can more readily react and connect with other fluorocarbon ions or fragments to grow polymer-like structures than smaller fragments, as shown in Figure 6. As a point of comparison, F atoms, the most dominant species in CF_3^+ deposition, deactivate an active site in the PS once it forms a chemical bond. Thus, these simulations predict that CF_3^+ deposition is more effective than $C_3F_5^+$ deposition in short-term treatments at fluorinating PS surfaces but $C_3F_5^+$ deposition might be more effective at growing fluorocarbon polymer layers for long-term processes.

Conclusions

This computational study investigates the reaction mechanisms that result in the chemical modification of PS surfaces through $C_3F_5^+$ and CF_3^+ ion beam deposition. The study uses classical MD simulations with a newly developed C–H–F empirical potential that is based on the second-generation REBO potential for hydrocarbons. For CF_3^+ deposition, F atoms play the most important role in fluorinating the PS surface because the majority of them are covalently attached to the PS chains through the replacement of native H atoms or capping the end of broken chains. CF_2 fragments are also an important long-lived species. In contrast, F atoms are a minor byproduct, and

CF₂ fragments are the most dominant species for C₃F₅⁺ deposition on PS. The simulations thus predict that CF₃⁺ deposition is more effective than C₃F₅⁺ deposition for polymer fluorination on the time scale of these simulations because of the large number of bare F atoms that are produced. In contrast, C₃F₅⁺ deposition might be more effective at producing precursors for fluorocarbon thin film growth for long-term process because of the larger sizes and greater functionality of the major ion fragments. Compared with real plasma or ion deposition processes, this simulation study explores only the very early stages of surface chemical modification and thin film growth, but the results indicate likely atomic-scale mechanisms responsible for these processes.

Acknowledgment. We gratefully acknowledge the support of the National Science Foundation (CHE-0200838).

References and Notes

- (1) Wheale, S. H.; Barker, C. P.; Badyal, J. P. S. *Langmuir* **1998**, *14*, 6699.
- (2) von Keudell, A. *Thin Solid Films* **2002**, *402*, 1.
- (3) Ada, E. T.; Kornienko, O.; Hanley, L. J. *J. Phys. Chem. B* **1998**, *102*, 3959.
- (4) Wijesundara, M. B. J.; Ji, Y.; Ni, B.; Sinnott, S. B.; Hanley, L. J. *Appl. Phys.* **2000**, *88*, 5004.
- (5) Cunge, G.; Booth, J. P. *J. Appl. Phys.* **1999**, *85*, 3952.
- (6) Wijesundara, M. B. J.; Hanley, L.; Ni, B. R.; Sinnott, S. B. *Proc. Natl. Acad. Sci. U.S.A.* **2000**, *97*, 23.
- (7) Jang, I.; Ni, B.; Sinnott, S. B. *J. Vac. Sci. Technol., A* **2002**, *20*, 564.
- (8) Jang, I.; Phillips, R.; Sinnott, S. B. *J. Appl. Phys.* **2002**, *92*, 3363.
- (9) Abrams, C. F.; Graves, D. B. *Thin Solid Films* **2000**, *374*, 150.
- (10) Abrams, C. F.; Graves, D. B. *J. Appl. Phys.* **2000**, *88*, 3734.
- (11) Abrams, C. F.; Graves, D. B. *J. Vac. Sci. Technol., A* **2001**, *19*, 175.
- (12) Alfonso, D. R.; Ulloa, S. E. *Phys. Rev. B* **1993**, *48*, 12235.
- (13) Smith, R.; Beardmore, K. *Thin Solid Films* **1996**, *272*, 255.
- (14) da Costa, M. E. H. M.; Freire, J.; F. L.; Jacobsohn, L. G.; Franceschini, D.; Mariotto, G.; Baumvol, I. R. J. *Diamond Relat. Mater.* **2001**, *10*, 910.
- (15) Wang, J. H.; Chen, J. J.; Timmons, R. B. *Chem. Mater.* **1996**, *8*, 2212.
- (16) Cho, B. O.; Hwang, S. W.; Lee, G. R.; Moon, S. H. *J. Vac. Sci. Technol., A* **2001**, *19*, 730.
- (17) Butterbaugh, J. W.; Gray, D. C.; Sawin, H. H. *J. Vac. Sci. Technol., B* **1991**, *9*, 1461.
- (18) Takahashi, K.; Itoh, A.; Nakamura, T.; Tachibana, K. *Thin Solid Films* **2000**, *374*, 303.
- (19) Horie, M. *J. Vac. Sci. Technol., A* **1995**, *13*, 2490.
- (20) Hanley, L.; Lim, H.; Schultz, D. G.; Garbis, S.; Yu, C. W.; Ada, E. T.; Wijesundara, M. B. *J. Nucl. Instrum. Methods Phys. Res., Sect. B* **1999**, *157*, 174.
- (21) Brenner, D. W.; Shenderova, O. A.; Harrison, J. A.; Stuart, S. J.; Ni, B.; Sinnott, S. B. *J. Phys.: Condens. Matter* **2002**, *14*, 783.
- (22) Abell, G. C. *Phys. Rev. B* **1985**, *31*, 6184.
- (23) Tersoff, J. *Phys. Rev. B* **1988**, *37*, 6991.
- (24) Tersoff, J. *Phys. Rev. B* **1988**, *38*, 9902.
- (25) Brenner, D. W. *Phys. Rev. B* **1990**, *42*, 9458.
- (26) Brenner, D. W.; Harrison, J. A.; White, C. T.; Colton, R. J. *Thin Solid Films* **1991**, *206*, 220.
- (27) Williams, E. R.; Jones, G. C.; Fang, L.; Zare, R. N.; Garrison, B. J.; Brenner, D. W. *J. Am. Chem. Soc.* **1992**, *114*, 3207.
- (28) Qi, L. F.; Sinnott, S. B. *J. Vac. Sci. Technol., A* **1998**, *16*, 1293.
- (29) Alfonso, D. R.; Ulloa, S. E.; Brenner, D. W. *Phys. Rev. B* **1994**, *49*, 4948.
- (30) Hu, Y.; Sinnott, S. B. *Nucl. Instrum. Methods Phys. Res., Sect. B* **2002**, *195*, 329.
- (31) Hu, Y. H.; Sinnott, S. B. *Surf. Sci.* **2003**, *526*, 230.
- (32) Tanaka, J.; Abrams, C. F.; Graves, D. B. *J. Vac. Sci. Technol., A* **2000**, *18*, 938.
- (33) Abrams, C. F.; Graves, D. B. *J. Appl. Phys.* **1999**, *86*, 5938.
- (34) Dewar, M. J. S.; Zebisch, E. G.; Healy, E. F.; Stewart, J. J. P. *J. Am. Chem. Soc.* **1985**, *107*, 3902.
- (35) Dewar, M. J. S.; Zebisch, E. G. *J. Mol. Struct.: THEOCHEM* **1988**, *180*, 1.
- (36) Allen, M. P.; Tildesley, D. J. *Computer Simulation of Liquids*; Oxford University Press: New York, 1987.
- (37) Marynowski, M.; Franzen, W.; El-Batanouny, M.; Staemmler, V. *Phys. Rev. B* **1999**, *60*, 6053.
- (38) Briand, J. P.; Thuriez, S.; Giardino, G.; Borsoni, G.; Froment, M.; Eddrief, M.; Sebenne, C. *Phys. Rev. Lett.* **1997**, *79*, 2591.
- (39) Gray, D. C.; Sawin, H. H.; Butterbaugh, J. W. *J. Vac. Sci. Technol., A* **1991**, *9*, 779.
- (40) Mackie, N. M.; Venturo, V. A.; Fisher, E. R. *J. Phys. Chem. B* **1997**, *101*, 9425.
- (41) Inayoshi, M.; Ito, M.; Hori, M.; Goto, T.; Hiramatsu, M. *J. Vac. Sci. Technol., A* **1998**, *16*, 233.
- (42) Nakamura, M.; Hori, M.; Goto, T.; Ito, M.; Ishii, N. *J. Vac. Sci. Technol., A* **2001**, *19*, 2134.
- (43) Koppers, W. R.; Gleeson, M. A.; Lourenco, J.; Weeding, T. L.; Los, J.; Kleyn, A. W. *J. Chem. Phys.* **1999**, *110*, 2588.
- (44) Koppers, W. R.; Beijersbergen, J. H. M.; Weeding, T. L.; Kistemaker, P. G.; Kleyn, A. W. *J. Chem. Phys.* **1997**, *107*, 10736.
- (45) Ast, T.; Riederer, D. E.; Miller, S. A.; Morris, M.; Cooks, R. G. *Org. Mass Spectrom.* **1993**, *28*, 1021.